




Cite this: DOI: 10.1039/d5na00741k

# Phase-locked random lasing in patterned microstripes of MAPbBr<sub>3</sub> porously structured with nanoholes

Yuxin Zhang, Qin Zhang and Xinping Zhang  \*

Mode locking is rarely observed in random lasing devices, as they are based on the strong optical scattering by random nanostructures and the requirement for strong nonlinear interactions in conventional mode-locking mechanisms cannot be satisfied in them. Our discovery of the cascaded absorption and stimulated emission (CASE) effect solved this challenge, with the strong overlap between the absorption and emission spectra in hybrid organic–inorganic perovskites being the underlying physics. Previously, phase-locked random lasing was observed in randomly distributed crystalline nanoparticles, which provide strong optical scattering and facilitate gain mechanisms for random lasing. In this work, we demonstrate phase-locked random lasing in continuous crystalline microstripes embedded with nanoholes. These nanoholes enable the formation of porous stripes of the active material, implying a different mechanism for random lasing. Microchannels with different widths were produced by photolithography using mask gratings with different periods and the same duty cycle of 50%. Microstripes were then created by spin-coating the green-emitting MAPbBr<sub>3</sub> precursor solution onto the mask gratings. Thus, nanohole-structured MAPbBr<sub>3</sub> microstripes formed in the grating grooves. Using femtosecond transient absorption spectroscopy, we were able to resolve the CASE features through the oscillations in the TA dynamics, which have a period of less than 400 fs. Phase-locked random lasing modes were identified by equally spaced spectral lines with a mode separation of 1.26–1.58 nm. Thus, phase-locking mechanisms for random lasers were verified in a nanoporous scheme.

Received 5th August 2025  
Accepted 22nd September 2025

DOI: 10.1039/d5na00741k

rsc.li/nanoscale-advances

## 1. Introduction

Based on the rapid development of new semiconductors and micro–nano preparation technologies, the study of random lasers<sup>1–4</sup> presents a development trend towards increasingly enriched material systems, advanced technical methods, and continually innovative photophysics. Mode control is one of the most important aspects of stochastic laser research. By utilizing the dependence of liquid crystal molecule birefringence on temperature changes, the temperature tuning characteristics of random lasers have been achieved.<sup>5</sup> The feedback mechanism provided by plasmonic optical scattering significantly broadens the construction methods of random laser devices.<sup>6</sup> White-light-emitting random lasers composed of multi-color mixtures offer advantages for applications in speckle free imaging and other fields.<sup>7</sup> Inkjet printing technology greatly enhances the flexibility and promotes the practical application of such devices.<sup>8</sup> Optical fiber based random lasers have become an important direction in this research field,<sup>9</sup> significantly enhancing the application of random lasers in new sensing and detection technologies.<sup>10</sup> The implementation of electrically pumped

random laser emission has created more opportunities for the development and application of such laser sources.<sup>11,12</sup>

Mode locking of random lasers has been a big challenge, as the essential characteristics of random laser emission make it is difficult to achieve the strong nonlinear optical effects required by conventional mode locking mechanisms. Two different random laser emission mechanisms were obtained by immersing clusters of titanium dioxide nanoparticles into a dye solution and by changing the shape of the pump beam. Based on experimental data, numerical calculations were conducted using coupled wave theory, and it is believed that this is a transition process towards mode locking,<sup>13</sup> which is considered a signature of forward mode locking.<sup>14</sup> Further research was conducted on the influence of different pump pulse widths on random laser emission modes, and numerical simulations were performed on the interactions between these modes using coupled wave theory.<sup>15</sup> Through statistical mechanical analysis and numerical simulation of the time integration of random laser emission spectra at different positions in GaAs crystal powder, the nonlinear coupling characteristics between random laser emission modes were theoretically demonstrated.<sup>16</sup> The statistical analysis of spectral intensity fluctuations confirmed its quasi Lévy distribution near the random laser threshold, while RSB analysis identified phase changes in

School of Physics and Optoelectronic Engineering, Beijing University of Technology, Beijing 100124, China. E-mail: zhangxinping@bjut.edu.cn



the order parameters corresponding to random laser initiation, thus confirming the coherent feedback mechanism of random laser emission in subwavelength quasi two-dimensional perovskite films.<sup>17</sup>

Recently, we reported cascaded absorption and stimulated emission (CASE) as a new mechanism for mode locking of lasers, which has been applied successfully in the phase-locking of random lasers using hybrid organic inorganic perovskites (HOIPs).<sup>18,19</sup> HOIPs provide a new material system for random lasers,<sup>20–24</sup> where the nanocrystalline particles in the HOIP polycrystalline thin films serve as both the gain media and the light scattering mechanisms, facilitating multiple advantages in the design of new random lasers. In particular, the overlapping between the absorption and emission spectra is the main physical basis for achieving cascaded absorption and stimulated emission (CASE) dynamics, which is crucial for achieving phase locking of the corresponding random lasers.

The CASE dynamics are characteristic of the periodic oscillation modulated on the transient absorption dynamics. The most important signature of phase-locking operation is the equally separated lasing lines. All of these effects are based on the strongly overlapping absorption and photoluminescence spectra. However, the reported phase-locked random lasers have been constructed from randomly arranged nanocrystals of HOIPs, where the boundaries between the nanocrystals provide optical scattering interfaces for gain interactions between the random lasing lines and the active nanocrystals. In this work, we demonstrate a new design and fabrication of phase-locked random lasers, where we patterned the HOIPs into continuous microstripes of high quality; however, nanoholes were embedded into the microstripes to provide the optical scattering mechanisms. Experimental results demonstrate strong signatures for both the CASE and the phase-locking effects, verifying the universally applicable principles for the phase-locking of random lasers.

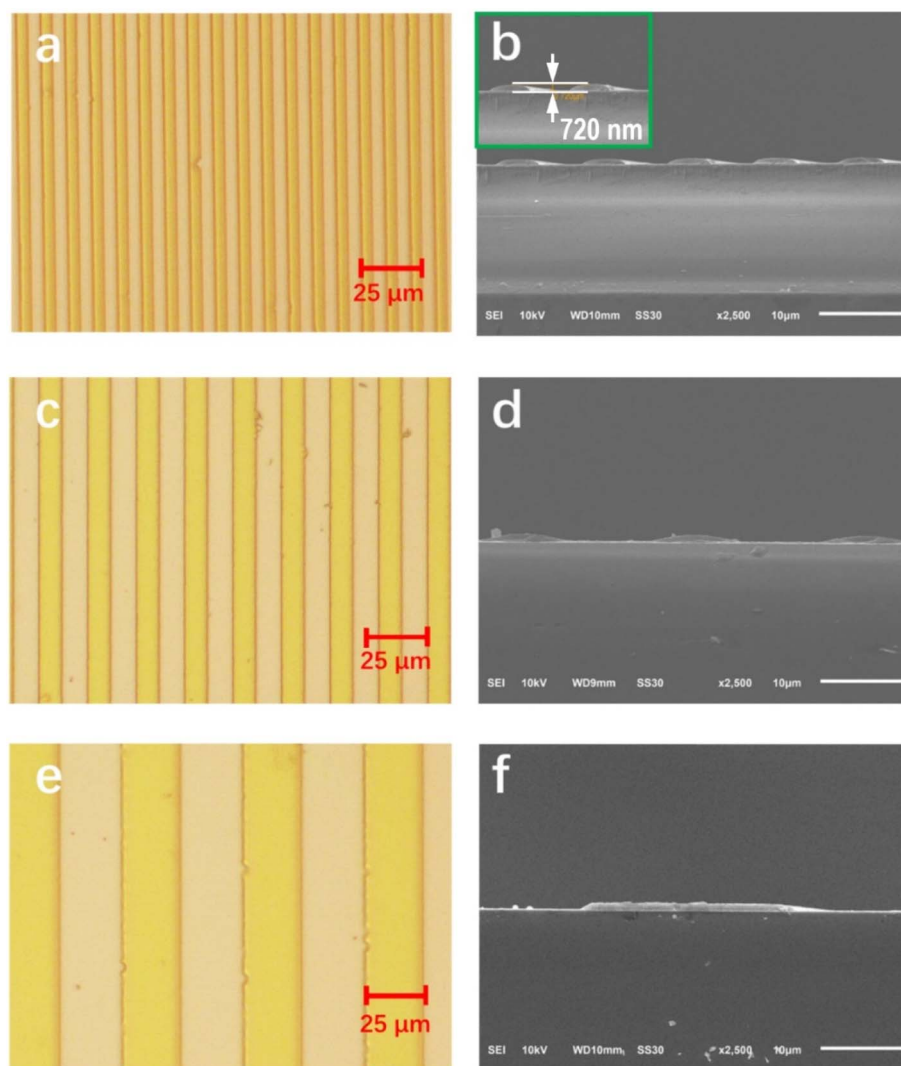


**Fig. 1** The top-view optical microscope (a, c and e) and the cross-sectional SEM (b, d and f) images of PR gratings prepared using photolithography with a period of 10 (a and b), 20 (c and d), and 50  $\mu\text{m}$  (e and f).



## 2. Fabrication of the micro-channel templates

Photolithography using ultraviolet exposure of a photoresist (PR) thin film produces the templates for the preparation of patterned microstripes of MAPbBr<sub>3</sub>, as shown in Fig. 1. Positive photoresist S1805 was purchased from Rohm & Haas Electronic Materials Ltd and it was spin-coated onto the surface of ITO glass using a spin-coating speed of 2000 rpm and a spin time of 30 s to produce the PR thin film. The sample was then placed on a 100 °C hot plate for 1 minute to remove residual solvents. During UV exposure, chromium photomasks with periods of 10, 20, and 50 μm and a duty cycle of 50% were employed. The samples were exposed to a UV light source at 365 nm for a duration of 15 s before the development process.

Fig. 1 shows the fabrication results for three different grating periods of 10, 20, and 50 μm. Fig. 1(a) shows the top-view optical microscope image of the PR grating with a period of 10 μm and Fig. 1(b) shows the cross-sectional scanning electron microscope (SEM) image. Clearly, the PR grating has a duty cycle of roughly 50% and a modulation depth of 720 nm. The modulation depth is equal to the thickness of the spin-coated PR thin film, which is basically the same for all fabricated gratings.

Fig. 1(c) and (d) show the microscopic images of the fabricated structures with a period of 20 μm, and Fig. 1(e) and (f) show those for a period of 50 μm. The duty cycle remains 50%; however, the modulation depth increases to more than 950 nm. The fabrication results show excellent homogeneity of the grating lines. These deep grating grooves provide micro-channels for the fabrication of MAPbBr<sub>3</sub> stripes in the subsequent procedures.

## 3. Random nanostructures in the active microstripes for optical scattering

In the fabrication of patterned stripes of MAPbBr<sub>3</sub>, we first prepare the precursor solution, where 60.78 mg MABr and 199.23 mg PbBr<sub>2</sub> are dissolved in 1 mL DMF solvent. Then, the mixture is stirred overnight on a magnetic stirrer, ensuring complete dissolution and formation of a homogeneous solution. The MAPbBr<sub>3</sub> precursor solution is spin-coated onto the above prepared photoresist grating, employing a two-stage process. In the first stage, the speed is set to 500 rpm for 5 s. Then, a spin speed of 4000 rpm for 40 s was set in the second stage; meanwhile, a small amount of antisolvent chlorobenzene is dripped onto the top surface of the sample to improve perovskite patterning and crystallization quality.

A series of experiments showed that excessively large channel widths in the template PR grating is not suitable for the preparation of continuous multi-crystalline stripes of MAPbBr<sub>3</sub>. For instance, when the grating period is increased to 50 μm, spin-coated MAPbBr<sub>3</sub> cannot produce continuous stripes; instead, isolated particles are randomly distributed within the grating grooves, as shown in Fig. S1. This implies uncontrollability of the fabrication process and the resultant structures for

a grating period as large as 50 μm. During spin-coating of the MAPbBr<sub>3</sub> precursor solution, the width of the grating grooves is a critical factor in determining the quality of the produced nanocrystal structures. When the grating period reaches 50 microns, the corresponding groove width is as large as 25 microns, if assuming a 50% duty cycle. In such cases, the precursor solution tends to flow toward the edges due to surface tension, resulting in uneven distribution within the grooves. Meanwhile, the wider grooves provide weaker confinement of the solution, leading to a much reduced amount of solution that is available for crystallization. As a result, no continuous structures can be produced in such wide grooves, as demonstrated in Fig. S1.

Therefore, we employed two grating periods of 10 and 20 μm for subsequent investigations. For a grating period of 10 μm, Fig. 2(a) and (b) show the optical fluorescence microscopy and scanning electron microscopy (SEM) images, respectively, of the MAPbBr<sub>3</sub> microstripes patterned within the photoresist gratings. Continuous and homogeneous stripes with a width of about 6.4 μm and a length of 2 cm were prepared, with a thickness smaller than 720 nm. When the grating period is increased to 20 μm, the width of the stripes becomes 12 μm, as shown in Fig. 2(c) and (d). Both samples show high-quality microstripes of the active MAPbBr<sub>3</sub> polycrystals.

According to above descriptions, the following factors are responsible for achieving high-quality microstripes: (1) The width of the grating grooves. The optimized width of the grooves ensures a sufficient amount of precursor solution and appropriate surface-tension interaction with the patterning surface, so that the precursor solution fully fills the channels. (2) The addition of a drop of the antisolvent chlorobenzene during the spin-coating process. Chlorobenzene is a non-polar and low-volatility solvent with a high-boiling point, so it hardly dissolves in the precursor solution. At the nucleation stage, chlorobenzene penetrates into the gaps between adjacent crystal grains, promoting the rapid crystallization of polycrystalline films. This regulates the crystallization process, optimizes grain size and morphology, and improves patterning quality. (3) The design of the spin-coating process. A low spin-coating speed not only maintains a sufficient amount of precursor solution in the grooves, but also slows down the solvent evaporation rate, thereby improving the crystallization quality and surface morphology of the microstripes. Furthermore, no annealing treatment was applied to the patterned samples after the spin-coating process; instead, the remaining solvent evaporated naturally, providing additional conditions for improving crystallization quality.

Nevertheless, small holes are observed to be distributed randomly within the microstripes, producing a porous structure. Such a scheme facilitates the main optical scattering mechanism for the random lasers in the patterned stripes. The inset of Fig. 2(d) shows an enlarged view of a local area of the MAPbBr<sub>3</sub> microstripe marked by a red rectangle. We measured a mean diameter of about 230 nm for the nanoholes constituting the porous structures, as highlighted by the yellow dashed circle. An average separation between the nanoholes is larger than 500 nm. The porous structures, in combination with



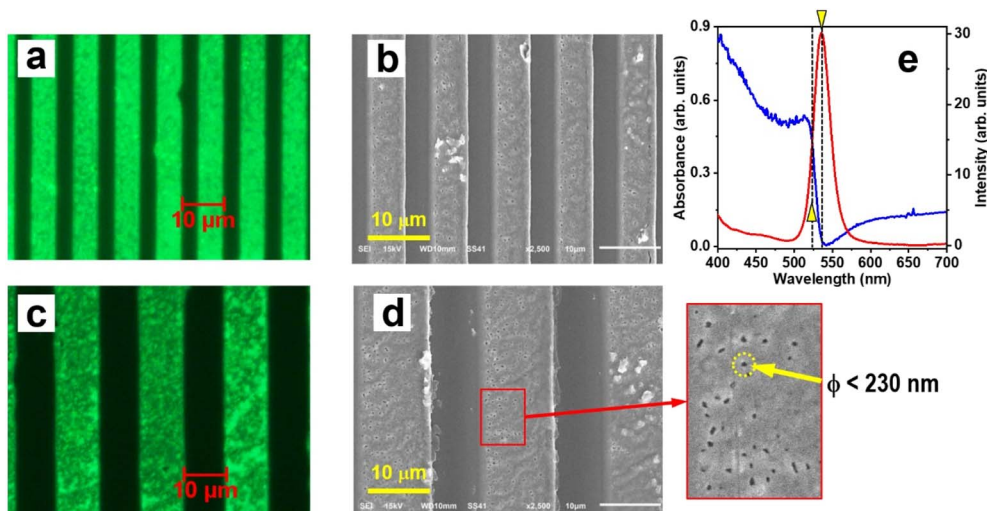


Fig. 2 (a and b) Optical microscopy and scanning electron microscopy (SEM) images, respectively, of the patterned MAPbBr<sub>3</sub> stripes fabricated using a photoresist grating with a period of 10 μm. (c and d) Optical microscopy and SEM images, respectively, of the patterned MAPbBr<sub>3</sub> stripes fabricated using a photoresist grating with a period of 20 μm. The inset of (d) shows an enlarged view of the porous structures on a local area of the MAPbBr<sub>3</sub> stripe, showing a rough hole diameter of about 230 nm. (e) Absorption (blue) and photoluminescence (red) spectra measured on the patterned MAPbBr<sub>3</sub> stripes.

the multi-crystalline configuration of the MAPbBr<sub>3</sub> stripes, are responsible for the optical scattering mechanisms for random lasing processes.

Fig. 2(e) shows the absorption (blue curve) and photoluminescence (red curve) spectra of the patterned MAPbBr<sub>3</sub> stripes, which differ little from those of thin films. As we have discovered for the phase-locking mechanisms, the cascaded absorption and stimulated emission is the responsible process, which is based on the large overlap between the absorption and emission spectra, as can be also be seen in Fig. 2(e). The strongest overlap occurs at the falling edge of the absorption spectrum and the rising edge of the emission spectrum; meanwhile, the peak of the photoluminescence (PL) spectrum overlaps with the dip in the absorption spectrum, as highlighted by the dashed vertical lines on the left and right, respectively. According to such features, we can also conclude that the PL spectrum results from self-absorption modulation, forming the basis for CASE mechanisms.

#### 4. Ultrafast dynamics by cascaded absorption and emission

Fig. 3(a) shows the energy-level diagram and electronic transition processes that may be involved in the transient absorption (TA) scheme in MAPbBr<sub>3</sub>. The pump pulse at  $h\nu_{\text{pump}}$  excites the ground-state (VB) molecules to the excitation band (CB), populating the lower edge of the CB. Interaction between the excited molecules and the probe pulse at  $h\nu_{\text{probe}}$  mainly includes excitonic absorption (positive TA) of the probe pulses for transitions to higher-lying states and amplification (negative TA) of the probe pulses through stimulated emission. Furthermore, strong excitation also reduces absorption of the probe pulses by the ground-state molecules, which is defined as

bleached ground-state absorption (negative TA). These processes are responsible for the overall TA dynamics.

In the TA measurements, a Ti:sapphire amplifier generated 150 fs pulses at 800 nm with a repetition rate of 1 kHz. A small portion of the pulses was sent through a cuvette containing heavy water with a thickness of 3 mm to produce super-continuum pulses, which were used as the probe. The remaining 800 nm pulses were frequency-doubled using a BBO crystal and the produced 400 nm pulses were used as the pump. The delay between the pump and probe pulses was adjusted by a linear translation stage with a time resolution of 1 fs, allowing a total delay range of 1 ns. Fig. 3(b) shows a 3D plot of the TA signal as a function of wavelength and time delay, where yellow-to-red colors denote positive TA and blue-to-green colors correspond to negative TA. Obvious oscillation dynamics between positive and negative TA can be observed between 492 and 552 nm, as highlighted by the dashed horizontal lines in Fig. 3(b). For a delay longer than  $\sim 1$  ps, the TA signal becomes negative over the whole dynamic curve, which corresponds to stimulated emission or bleached ground-state absorption, as highlighted by the dashed vertical line.

Fig. 3(c) shows the TA spectra at delays of 0 (start of overlap between the pump and probe pulses), 0.1, 0.4, 2, 10, and 900 ps, where two negative dips are observed at 522 (green triangle) and 545 nm (yellow triangle), and a positive peak is located in between at about 537 nm. The negative TA feature at 522 nm results mainly from the bleached ground-state absorption, as highlighted by the green triangles, whereas, the one at 545 nm is dominated by stimulated emission. Although the positive signal is observed to be centered at about 537 nm and lasts less than 400 fs, it is a broadband signal extending from 450 to longer than 650 nm and results from exciton absorption. The competition between the positive exciton absorption and the





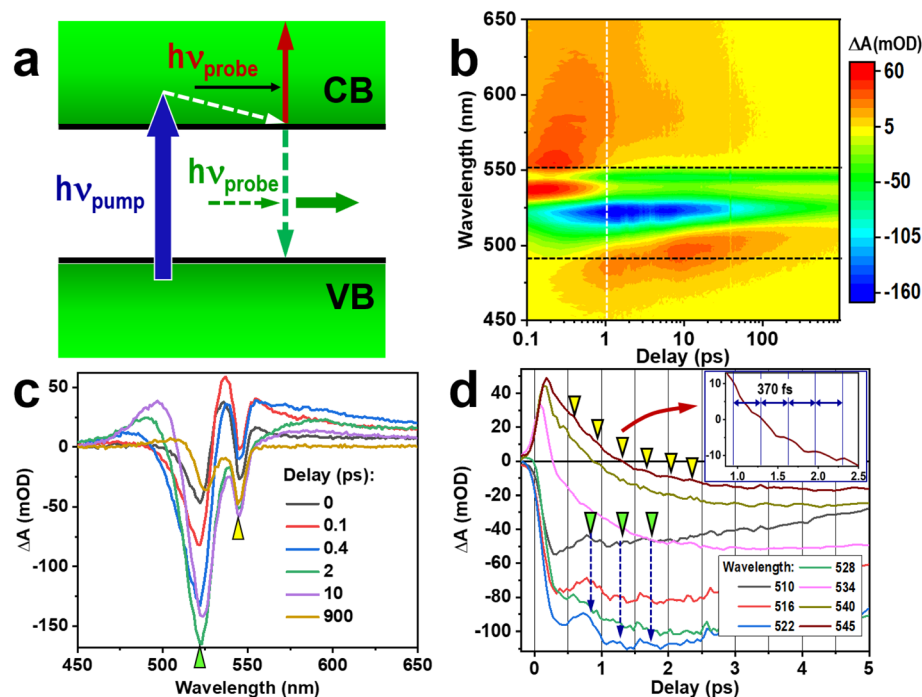


Fig. 3 (a) Energy-level illustration of the pump–probe scheme for the investigation of the phase-locking mechanism. (b) Transient absorption (TA) signal  $\Delta A$  as a function of wavelength and time delay. (c) TA spectra at delays of 0, 0.1, 0.4, 2, 10, and 900 ps. (d) TA dynamics at wavelengths of 510, 516, 522, 528, 534, 540, and 545 nm. Inset: TA dynamics at 545 nm, showing an oscillation with a period of about 370 fs.

relatively narrow-band bleaching and stimulated emission processes produces the spectral structures in Fig. 3(c). Such an interaction is responsible for the CASE effect, which is observed as oscillations in the TA dynamics, as shown in Fig. 3(d). The CASE effect originates from the overlap between the absorption and emission spectra of MAPbBr<sub>3</sub>. After excitation by a pump pulse with photon energy larger than the bandgap, intraband transition takes place quickly to the edge of the conduction band after a delay of  $\Delta\tau$ . If the emission through interband transition also falls within the absorption band, it will excite ground-state molecules again efficiently. Similarly, after a cascading relaxation time of  $\Delta\tau$ , emissive transition produces secondary photons with similar energies. Due to the constant lifetime  $\Delta\tau$ , a fixed phase-shift of  $\Delta\phi$  is introduced into the cascading processes, providing the basis for phase locking of these lasing modes. Meanwhile, cascaded emission supplies correlated injections between different random lasing channels, strengthening the phase-locking mechanism.<sup>18</sup>

Fig. 3(d) shows a series of TA dynamics at 510, 516, 522, 528, 534, 540, and 545 nm, where the CASE-induced oscillation can be observed for all of the dynamics curves, although the amplitude of the oscillation is weak for some curves. The oscillation features are highlighted by triangles and indicated by the dashed vertical lines, showing an oscillation period of about 400 fs. For the dynamics at 545 nm, corresponding to the peak wavelength of stimulated emission, the oscillation period is measured to be shorter than 360 fs, as locally enlarged in the inset of Fig. 3(d). The oscillation in the TA dynamics verifies the CASE mechanism and provides the basis for phase-locked

random lasing. The difference in oscillation periods between wavelengths shorter than 528 nm and those longer than 540 nm actually distinguishes the ground-state bleaching effect from the CASE mechanism.

## 5. Phase-locked random lasing performance

Fig. 4(a) shows the micro-spectroscopic system schematically for characterizing the phase-locking properties of random lasing in the patterned MAPbBr<sub>3</sub> microstrips. 150 fs laser pulses at 800 nm were first frequency-doubled in a BBO crystal, producing 400 nm pulses as the pump for random lasers. The 400 nm pulses were converged by the focusing lens into an objective, so that these pump pulses were focused into the active microstructures of MAPbBr<sub>3</sub> after being reflected by a dichroic mirror. The lasing emission was collected by the objective and transmitted to the spectrometer after passing through the dichroic mirror.

Fig. 4(b) shows the SEM images of the samples that were investigated for phase-locked random lasing performance, where two grating periods of  $\Lambda = 10\ \mu\text{m}$  (left) and  $20\ \mu\text{m}$  (right) were employed for the fabrication of active microstrips. The pump laser was focused onto an area with a diameter of about  $20\ \mu\text{m}$  on the surface of the sample, as marked by the dashed circles in Fig. 4(b). Compared with our previous publications,<sup>18,19</sup> nanohole or porous structures in continuous micro-channels, instead of nanocrystalline particles, constitute the optical scattering mechanisms for random lasing. In principle,



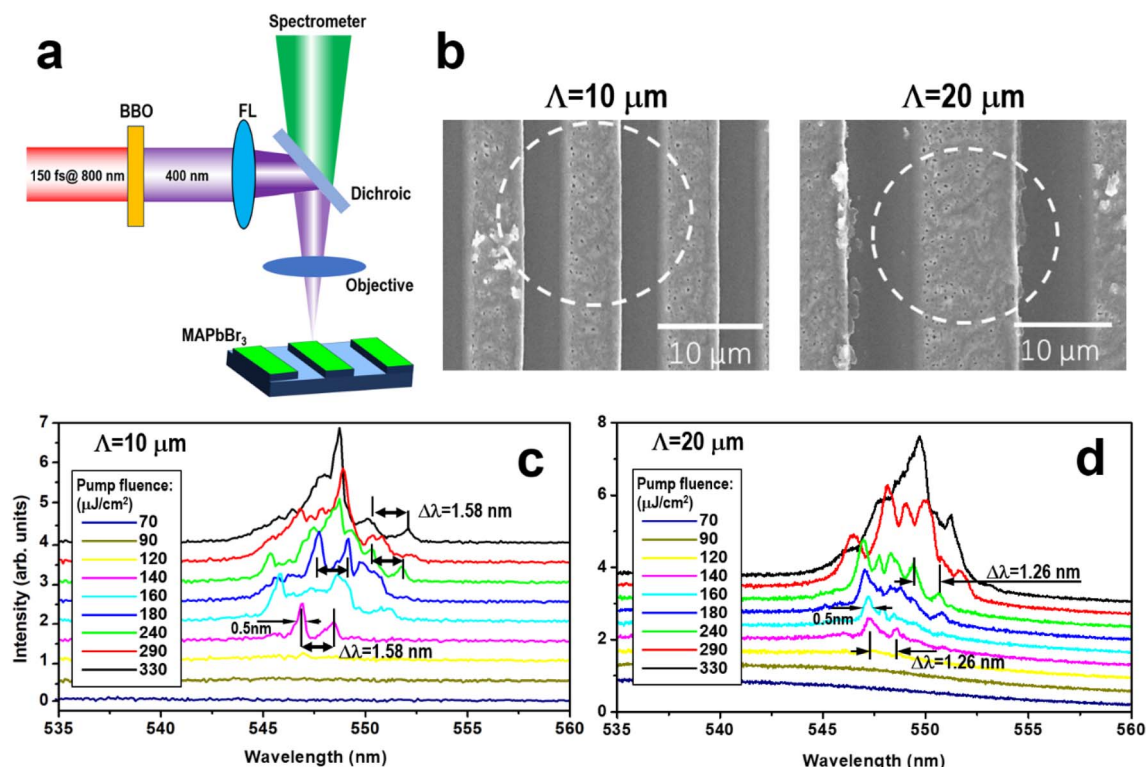


Fig. 4 (a) The micro-spectroscopic system for investigating the phase-locked random lasing performance. (b) SEM images for the micro-grating patterned MAPbBr<sub>3</sub> channels with a period of  $\Lambda = 10$  (left) and  $\Lambda = 20 \mu\text{m}$  (right). (c and d) Phase-locked random lasing spectra at varied pump fluences for  $\Lambda = 10$  and  $20 \mu\text{m}$ , respectively.

such a configuration actually reduces the strength of optical scattering, consequently increasing both the lasing and the phase-locking thresholds. The corresponding phase-locked random lasing properties are shown in Fig. 4(c) and (d) for  $\Lambda = 10$  and  $20 \mu\text{m}$ , respectively.

Fig. 4(c) shows the phase-locked random lasing spectra at pump fluences ranging from 70 to 330  $\mu\text{J}/\text{cm}^2$ . A lasing threshold of about 120  $\mu\text{J}/\text{cm}^2$  can be determined from the spectroscopic characterization. Multiple peaks with roughly equal separations can be observed for all lasing spectra above the threshold, which can be justified as the phase-locked modes. Competition between these modes can be observed, with the mode centered at about 550 nm becoming the strongest at 330  $\mu\text{J}/\text{cm}^2$ . A mode separation of about 1.58 nm can be measured for all of the lasing spectra and a linewidth of about 0.5 nm can be measured for all modes. Such a mode separation corresponds to a cavity length of larger than 190  $\mu\text{m}$  if assuming a microcavity effect, which does not exist in the microchannel with a width of 5  $\mu\text{m}$ . Therefore, the equal spectral separation serves as a signature of the phase-locking effect between multiple working modes.

The same characteristic features can also be observed for the sample having a grating period of 20  $\mu\text{m}$  and a channel width of about 10  $\mu\text{m}$ , as shown in Fig. 4(d). As has been investigated in our previous publication,<sup>18</sup> a larger multi-crystalline channel enhances the randomness and reduces the phase-locking strength, so that the equal mode-separation

mechanism becomes weaker and linewidth of each mode becomes larger. This can be observed from the comparison between Fig. 4(c) and (d). A mode separation of 1.26 nm can be observed in Fig. 4(d) with a linewidth as narrow as 0.5 nm. The strongest lasing mode is also observed at about 550 nm for a pump fluence of 330  $\mu\text{J}/\text{cm}^2$ . The threshold for lasing actions remains almost the same for both structures. In fact, the number of phase-locked lasing lines is mainly determined by the intraband transition lifetime, as has been investigated in ref. 18. It is in principle not dependent on the pump fluence. However, the weak lasing lines are not obviously identified at low pump fluences; therefore, the number of visible lasing lines increases with increasing pump fluence. Since there is a shift of the lasing lines due to the interaction between emission and ground-state bleaching with increasing pump fluence, the number of lasing lines may also change on such basis; however, this is not a monotonic process.

As a comparison, we carried out experiments using a common optical system, as shown in Fig. S2. The pump laser beam was sent to the sample using a simple focusing lens with a focal length of 150 mm; however, the sample was not placed on the focal plane in the practical measurement, so that the pump laser beam had a diameter of about 3 mm on the surface of the sample. Fig. S3 shows the emission spectra at varied pump fluences. Single-peak random lasing spectra were measured for devices with periods of 10 and 20  $\mu\text{m}$ ; however, the lasing spectrum is centered at 550 nm with a linewidth of



6.2 nm for the 10  $\mu\text{m}$  grating period and at about 545.4 nm with a linewidth of 6.8 nm for the 20  $\mu\text{m}$  period. Therefore, the narrow linewidth of the lasing mode provides further evidence for the phase-locking effect.

Furthermore, we note that for similarly sized microstructures, the nanohole scheme showed a lower pump threshold for random lasing than the nanoparticle scheme in ref. 18. This is because the nanohole scheme provides better confinement of the emission into the continuous microstrips than the nanoparticles, whereas the isolated nanoparticles introduce stronger optical-scattering loss. Meanwhile, we also note that the size, the density, and the total number of the nanoholes are smaller than those of the nanoparticles; consequently, the weakened scattering process reduces the interaction strength and mode selectivity for nanohole structures. Therefore, relatively larger full linewidths, lower contrast, and reduced distribution periodicity of the lasing lines can be observed in Fig. 3(d), as compared with the nanoparticle scheme. Additionally, the above mechanisms also led to larger irregularity and asymmetry in the spectra of the lasing lines for the nanohole structures compared with the nanoparticles.

## 6. Conclusions

We investigated the phase-locking performance of the random laser emission in patterned MAPbBr<sub>3</sub>, where the grooves of the PR grating were used as the template to confine the active materials into microstrips. Random structures form in the continuous microstrips as nanoholes with a mean diameter of about 230 nm, which are an inverted structure compared to the common nanoparticle scheme and provide optical scattering mechanisms for random lasing. Phase-locked lasing modes are observed as multiple lasing lines in the green with equal separations in the spectral range from 540 to 555 nm. The CASE effect is responsible for the phase locking and is verified by oscillations in the TA dynamics with a period less than 400 fs. The results not only provide new insights into the photophysics for the phase-locking of random lasers using nanohole structures, but also more solidly verify CASE-based phase-locking as a universally applicable mechanism.

## Conflicts of interest

The authors declare no competing interests.

## Data availability

The data supporting this article have been included as part of the SI. Supplementary information is available. See DOI: <https://doi.org/10.1039/d5na00741k>.

## Acknowledgements

The authors acknowledge the support by the National Natural Science Foundation of China (12574406).

## References

- 1 H. Cao, Y. G. Zhao, S. T. Ho, *et al.*, Chang, Random laser action in semiconductor powder, *Phys. Rev. Lett.*, 1999, **82**, 2278.
- 2 H. Cao, J. Y. Xu, S. H. Chang, *et al.*, Transition from amplified spontaneous emission to laser action in strongly scattering media, *Phys. Rev. E*, 2000, **61**, 1985.
- 3 B. Redding, A. A. Choma and H. Cao, Speckle-free laser imaging using random laser illumination, *Nat. Photonics*, 2012, **6**, 355.
- 4 D. Wiersma, The smallest random laser, *Nature*, 2000, **406**, 132.
- 5 D. S. Wiersma and S. Cavaleri, A temperature-tunable random laser, *Nature*, 2001, **414**, 708.
- 6 T. Zhai, X. Zhang, Z. Pang, *et al.*, Random laser based on waveguided plasmonic gain channels, *Nano Lett.*, 2011, **11**, 4295.
- 7 S. W. Chang, W. C. Liao, Y. M. Liao, *et al.*, A white random laser, *Sci. Rep.*, 2018, **8**, 2720.
- 8 Y. M. Liao, W. C. Liao, S. W. Chang, *et al.*, Inkjet-printed random lasers, *Adv. Mater. Technol.*, 2018, **3**, 1800214.
- 9 C. J. S. de Matos, L. de S. Menezes, A. M. Brito-Silva, *et al.*, Random fiber laser, *Phys. Rev. Lett.*, 2007, **99**, 153903.
- 10 E. Iguesti, F. Tommasi, L. Fini, *et al.*, A new class of optical sensors: a random laser based device, *Sci. Rep.*, 2016, **6**, 35225.
- 11 S. F. Yu, Electrically pumped random lasers, *J. Phys. D: Appl. Phys.*, 2015, **48**, 483001.
- 12 B. Meng, G. Liang, J. Tao, *et al.*, Electrically pumped mid-infrared random lasers, *Adv. Mater.*, 2013, **25**, 6859.
- 13 M. Leonetti, C. Conti and C. Lopez, The mode-locking transition of random lasers, *Nat. Photonics*, 2011, **5**, 615.
- 14 H. Kalt, Towards mode-locking, *Nat. Photonics*, 2011, **5**, 573.
- 15 M. Leonetti, C. Conti and C. Lopez, Dynamics of phase-locking random lasers, *Phys. Rev. A*, 2013, **88**, 043834.
- 16 F. Antenucci, G. Lerario, B. S. Fernandez, *et al.*, Demonstration of Self-Starting Nonlinear Mode Locking in Random Lasers, *Phys. Rev. Lett.*, 2021, **126**, 173901.
- 17 C. Fruhling, K. Wang, S. Chowdhury, *et al.*, Coherent random lasing in subwavelength quasi-2D perovskites, *Laser Photonics Rev.*, 2023, **17**, 2200314.
- 18 X. P. Zhang, J. Y. Hu, Y. L. Fu, *et al.*, Phase-locking of random lasers by cascaded ultrafast molecular excitation dynamics, *Laser Photonics Rev.*, 2023, **17**, 2200333.
- 19 Q. Zhang, Y. Liu, Y. Zhang, *et al.*, Two-photon pumped phase-locking of random lasers in hybrid perovskite microcrystalline microdisks, *Ultrafast Sci.*, 2024, **4**, 0068.
- 20 R. Dhanker, A. N. Brigeman, A. V. Larsen, *et al.*, Random lasing in organo-lead halide perovskite microcrystal networks, *Appl. Phys. Lett.*, 2014, **105**, 151112.
- 21 Y. Liu, W. Yang, S. Xiao, *et al.*, Surface-emitting perovskite random lasers for speckle-free imaging, *ACS Nano*, 2019, **13**, 10653.
- 22 A. O. Murzin, B. V. Stroganov, C. Günnemann, *et al.*, Amplified spontaneous emission and random lasing in



- MAPbBr<sub>3</sub> halide perovskite single crystals, *Adv. Opt. Mater.*, 2020, **8**, 2000690.
- 23 Y. Zhang, B. Zhang, Y. Fu, *et al.*, Amplified spontaneous emission of perovskite in water: towards under-water lasing, *Mater. Today Phys.*, 2022, **24**, 100686.
- 24 J. Hu, M. Wang, F. Tang, *et al.*, Threshold size effects in the patterned crystallization of hybrid halide perovskites for random lasing, *Adv. Photonics Res.*, 2021, **2**, 2000097.

